

# The Active Site Structure of Tetanus Neurotoxin Resolved by Multiple Scattering Analysis in X-Ray Absorption Spectroscopy

C. Meneghini\*<sup>§</sup><sup>¶</sup> and S. Morante\*<sup>§</sup>

\*Laboratori Nazionali di Frascati INFN, 00044 Frascati, Italy; <sup>¶</sup>Dipartimento di Fisica, Università di Roma *Tor Vergata*, 00133 Rome, Italy; <sup>§</sup>Istituto Nazionale di Fisica della Materia Sezione B, Unità di Roma *Tor Vergata*, Rome, Italy; and <sup>¶</sup>Istituto Nazionale di Fisica della Materia, European Synchrotron Radiation Facility, Grenoble, France

**ABSTRACT** A detailed study of the x-ray absorption spectrum of tetanus neurotoxin in the *K*-edge EXAFS region of the zinc absorber is presented that allows the complete identification of the amino acid residues coordinated to the zinc active site. A very satisfactory interpretation of the experimental data can be given if multiple scattering contributions are included in the analysis. Comparing the absorption spectrum of tetanus neurotoxin to that of two other structurally similar zinc-endopeptidases, thermolysin and astacin, in which the zinc coordination mode is known from crystallographic data, we conclude that in tetanus neurotoxin, besides a water molecule, zinc is coordinated to two histidines and a tyrosine.

## INTRODUCTION

Tetanus neurotoxin (TeNT), together with botulinum, is the most powerful known natural toxin. In both cases the toxin is known (Montecucco and Schiavo, 1994; Simpson, 1989) to be the sole cause of the associated devastating diseases, tetanus and botulism, respectively. TeNT and the seven known different serotypes of botulinum have recently been shown to belong to the wider class of zinc-endopeptidases (Montecucco and Schiavo, 1993; Schiavo et al., 1992b). As their potency is mainly due to their very high degree of neurospecificity (Schiavo et al., 1992a), many efforts have been spent, in the last few years, in the attempt to characterize the structure of the zinc (Zn) active site (Minton, 1995; Lebeda and Olson, 1994). The understanding of intracellular activity can, in fact, throw light on the molecular origin of the disease and help researchers substantially in their efforts to devise new, more effective therapeutic strategies. In particular, to clarify the molecular basis of TeNT pathogenesis, it is necessary to arrive at the identification of the amino acid residues primarily bound (coordinated) to Zn.

X-ray absorption spectroscopy (XAS) is the ideal tool for selectively probing the local structure of a specific photoabsorber embedded in a medium, whether solid, liquid, or gas, even at very low concentration (as is often the case in instances of biological relevance).

At sufficiently high energies above threshold, the x-ray absorption spectrum presents oscillations (extended x-ray absorption fine structure, EXAFS) that are characteristic of the local structure around the absorber (Lee et al., 1981; Teo and Joy, 1981; Koningsberger and Prins, 1988).

Starting in the early 1970s (Sayers et al., 1971; Stern, 1974), detailed studies of the EXAFS high-energy region led to the resolution of the near structure around the absorber in many interesting cases in the field of condensed matter, chemistry, and biology with, however, the limitation that light atoms (like oxygen, carbon, and nitrogen) are rather difficult to distinguish from one another, because of the strong similarity of their back-scattering amplitudes and phase shifts (Teo and Joy, 1981; Koningsberger and Prins, 1988). As a result, when this spectroscopic technique was tried on biological systems, the simple treatment of the EXAFS signal, in terms of single scattering events only, turned out to be insufficiently refined to allow the identification of the amino acid residues coordinated to the metal in a metalloprotein, because the atom through which amino acids are bound to the metal (with the only exception of cysteine) is always a light one.

Soon after the work of Lee and Pendry (1975) and Ashley and Doniach (1975), new theoretical developments (Benfatto et al., 1986; Gurman et al., 1986; Fonda, 1992) have allowed the inclusion of multiple scattering (MS) contributions in the analysis of XAS data, leading to a much better understanding of both the EXAFS and the near edge (XANES) signals.

Information on the number, the type, and the geometrical arrangement around the absorber of nearby and more distant scattering centers (Strange et al., 1987; Bianconi et al., 1987; Filipponi et al., 1989; Zhang et al., 1997, and references therein) can be obtained by fits to experimental data that also include MS contributions. If a certain amount of further structural indications about the atomic environment around the absorber is available (e.g., from crystallographic data on similar compounds, from chemical or mutagenesis experiments, etc.), it may be possible to arrive at a clear-cut identification of the amino acids coordinated to the metal in the active site.

Recently (Morante et al., 1996) the x-ray absorption spectra of TeNT and of three related Zn-endopeptidases, two astacin-like enzymes (astacin and alkaline protease),

Received for publication 4 February 1998 and in final form 8 June 1998.

Address reprint requests to Dr. Silvia Morante, Dipartimento di Fisica, Università degli Studi di Roma *Tor Vergata*, Via della Ricerca Scientifica, 00133 Rome, Italy. Tel.: +39-6-72594554; Fax: +39-6-2023507; E-mail: morante@roma2.infn.it.

© 1998 by the Biophysical Society

0006-3495/98/10/1953/11 \$2.00

and thermolysin have been measured. Unlike the cases of thermolysin (Matthews et al., 1972), astacin (Bode et al., 1992), and alkaline protease (Baumann et al., 1993), there are no crystallographic data available for TeNT. TeNT experimental spectra were analyzed in the single scattering approximation, and compared with the spectra of the three other structurally similar Zn-endopeptidases. From this comparative study, a new pattern of Zn coordination mode in TeNT was suggested (Morante et al., 1996) in which, besides a water molecule and two histidines, a tyrosine is taken as a fourth Zn ligand. The possibility, however, of having Zn pentacoordinated with the inclusion of a glutamic acid could not be excluded.

The aim of this paper is to clarify the issue by unambiguously identifying the amino acids coordinated to Zn in TeNT from a careful discussion of the contributions of scatterings from atoms at distances from the absorber larger than the first coordination shell, where MS events cannot be ignored. This analysis leads to the conclusion that Zn is tetracoordinated, as first tentatively suggested by Morante et al. (1996).

To decode the large amount of structural information contained in MS patterns, experimental data with a very good signal-to-noise ratio on model compounds are also required. We then repeated the EXAFS measurements on thermolysin and astacin. The results of the fits performed on these two structurally known enzymes are in very good agreement with the structural configurations that emerge from crystallographic data, making us confident about the reliability of the results we obtain in the structurally unknown case of TeNT.

## MATERIALS AND METHODS

Astacin was isolated from the European freshwater crayfish *Astacus astacus* L., according to the method developed by Zwilling and Neurath (1981). Zn(II)-Astacin was prepared starting with the Zn free apo-enzyme, which was then dialyzed versus a 0.1 M buffered solution of Zn sulfate. The final astacin concentration, in 0.02 M Na/HEPES buffer at pH 8.1, was 0.6 mM. (We thank Dr. W. Stöcker for preparing the sample.) Thermolysin was obtained starting from a commercial Sigma preparation, which was further purified by the recrystallization method described by Matsubara (1970). The sample (25 mg) was suspended in 1 ml of ice-cold 0.02 M Ca-acetate, pH 7.0, and the pH of the suspension was then adjusted to 11.5 by dropwise addition of 0.2 M NaOH. After a brief centrifugation to remove possible residual precipitates, the pH of the solution was adjusted to 8.9 with 0.2 M CH<sub>3</sub>COOH (acidic acid), and the solution was left overnight in an ice bath. Crystals were then collected by centrifugation (9000 rpm for 10 min) and resuspended in 5 M NaBr, 0.01 M Ca-acetate, 0.05 M Tris-Cl, pH 7.5. The final protein concentration, determined using a molar extinction coefficient of 66,300 at 280 nm, was 0.84 mM. (We thank Dr. L. Castellani for preparing the sample.)

New XAS measurements on astacin and thermolysin were performed at the D8 GILDA (General Italian Line for Diffraction and Absorption) CRG beam-line at the European Synchrotron Radiation Facility (ESRF) in Grenoble. Spectra were recorded in fluorescence geometry at room temperature. At this temperature both samples were liquid and were held in a 3.0-mm-thick aluminum sample holder with 6 × 15 mm<sup>2</sup> kapton windows. Beam energy was defined using a Si(311) double crystal, sagittal focusing, and a monochromator (Pascarelli et al., 1996). The dynamical sagittal focusing concentrates the 4 mrad of horizontal source divergence to obtain

an intense focal spot on the sample, whose size (~2 mm) is kept constant during each scan. The incident photon flux,  $I_o$ , is measured with an ionization chamber, and the fluorescence photons,  $I_f$ , are recorded with a Ge solid-state detector.

We collected five thermolysin spectra and six astacin spectra for a total integration time of ~100 s/point and 200 s/point, respectively. Somewhat fewer statistics were collected in the case of thermolysin, because this enzyme undergoes an autodigestive process at room temperature, which we have continuously monitored and avoided by frequently renewing the sample. As a result, thermolysin single runs could not be too long. To improve the counting statistics, the experimental absorption signal on each sample was defined as

$$\mu_{\text{Abs}}(E) = \frac{1}{m} \sum_{i=1}^m \frac{I_f^{(i)}(E)}{I_o^{(i)}(E)} \quad (1)$$

where the sum is over the  $m$  repeated measurements. All of the spectra were collected in the incident photon energy range  $E = 9510$ – $10150$  eV.

The Zn EXAFS spectra of TeNT used in this paper are those collected at the X-19 beamline at the National Synchrotron Light (NSL) source of the Brookhaven National Laboratory (Morante et al., 1996). Data were sufficiently accurate for the purpose of the analysis presented here.

## DATA ANALYSIS

In XAS experimental settings, the incident photon energy must be sufficiently large to excite inner-shell electrons from the absorbing atoms with consequent sharp steps in the absorption intensity, as the x-ray energy is increased through an inner-shell ionization threshold.

The EXAFS region of the spectrum is characterized by a series of gentle oscillations that may be interpreted in terms of the scattering of the excited photoelectrons by the neighboring atoms (Lee et al., 1981; Teo and Joy, 1981; Koningsberger and Prins, 1988). The resulting interference of the reflected electron waves with the photo-electron spherical wave leaving the absorber leads to the observed modulation of the signal.

The EXAFS structural signal  $\chi(k)$  is defined as the relative deviation of the measured absorption coefficient,  $\mu_{\text{Abs}}$  (Eq. 1), with respect to the atomic absorption cross section,  $\mu_o$ , of the edge under consideration:

$$\chi(k) = \frac{\mu_{\text{Abs}}(k) - \mu_o(k)}{\mu_o(k)} \quad (2)$$

where

$$k = \frac{\sqrt{2m(E - E_0)}}{\hbar} \quad (3)$$

is the modulus of the wave vector of the photoelectron and  $E_0$  is the origin of its kinetic energy.

In the single scattering approximation  $\chi(k)$  can be expressed in terms of structural parameters through the formula

$$\chi(k) = \sum_s \left( \frac{N_s}{kR_{\text{AS}}^2} \right) F_s(k) \exp(-2k^2\sigma_{\text{AS}}^2) \exp\left(-\frac{2R_{\text{AS}}}{\lambda(k)}\right) \sin[2kR_{\text{AS}} + \delta_{\text{AS}}(k)] \quad (4)$$

valid in the EXAFS region, i.e., for large values of  $k$ . In Eq. 4,  $N_S$  is the number of scatterers of type  $S$  located at a distance  $R_{AS}$  from the absorber,  $A$ . Scatterers are assumed to have a Gaussian spatial distribution around their equilibrium position with mean square root deviation (width)  $\sigma_{AS}$ .  $F_S(k)$  is the modulus of the back-scattering amplitude, and  $\delta_{AS}(k)$  is the total scattering phase. ( $\delta_{AS}(k)$  is the sum of two terms: twice the phase of the central atom and the phase of the scattering atom.) The exponential  $\exp(2R_{AS}/\lambda(k))$  takes into account the finiteness of both the mean free path of the photoelectron and the core-hole life time, and kills contributions from distant atoms.

The analysis of the EXAFS data in the single scattering approximation is now a well-established method in the situation in which the relevant scattering centers are not too distant from the absorber (less than 3 Å; Lee et al., 1981; Teo and Joy, 1981; Koningsberger and Prins, 1988). Beyond this distance, MS contributions become important and may compete in magnitude with single scattering signals.

The importance of including MS contributions to provide a reliable and more accurate theoretical basis for EXAFS data analysis in biological samples has been emphasized in the study of metal-bonded imidazole complexes (Bunker et al., 1982; Blackburn et al., 1983), where MS contributions are strongly enhanced by the focusing effect coming from the nearly colinear configuration formed by the absorber in association with the nitrogen and the carbon of the imidazole ring.

This study has for the first time allowed the identification of an histidine residue, as one of the amino acids bound to the metal absorber in proteins (Strange et al., 1987).

In view of the large amount of information encoded in principle in the MS contributions to XAS (type, number, and geometrical arrangement of distant atoms), a great deal of theoretical effort has been spent in recent years to accurately describe and interpret MS processes (Benfatto et al., 1986; Gurman et al., 1986; Fonda, 1992).

In this paper we rely on the theoretical approach developed in the papers of Benfatto et al. (1986) and Filipponi et al. (1995a), which has been fully implemented in the freely available GNXAS package (Filipponi et al., 1995b).

The distinctive features of the treatment of Filipponi et al. (1995a) can be summarized as follows. 1) The usual MS expansion (Benfatto et al., 1986) (of which the expression in Eq. 4 is the first term) is replaced by an equivalent expansion in terms of irreducible  $n$ -body signals,  $\gamma^{(n)}$  (see below). The reason for this choice is that the latter expansion can be proved to have better convergence properties, because in each term infinitely many MS contributions are automatically summed up. 2) The effect of including MS events is consistently taken into account over the whole XAS, including the EXAFS region.

For the reader's convenience, we briefly recall here the main conceptual points of the approach we will follow and collect some useful formulae.

The novelty of the theoretical treatment advocated by Filipponi et al. (1995a) consists of expressing the absorption

coefficient as a sum of normalized  $n$ -body irreducible photoelectron cross sections,  $\sigma_l/\sigma_0$ , which are then evaluated in terms of quantum mechanical scattering amplitudes. Irreducible  $n$ -body cross sections,  $\sigma_l$ , are iteratively defined, starting from the 2-body case, in terms of the  $n$ -body complete cross sections,  $\sigma$ , via the equations

$$\begin{aligned}\sigma_1(A; 1) &= \sigma(A; 1) - \sigma_0(A) \\ \sigma_1(A; 1, 2) &= \sigma(A; 1, 2) - \sigma_1(A; 1) - \sigma_1(A; 2) - \sigma_0(A) \\ &\vdots \\ \sigma_1(A; 1, 2, \dots, S) &= \sigma(A; 1, 2, \dots, S) \\ &\quad - \sum_{C_S(i_1, \dots, i_{S-1})} \sigma_1(A; i_1, \dots, i_{S-1}) - \dots \\ &\quad - \sum_{C_S(i_1)} \sigma_1(A; i_1) - \sigma_0(A)\end{aligned}\quad (5)$$

where, as before,  $A$  stands for the absorber (central) atom, and the indices  $1, 2, \dots, S$  label the scattering centers involved in the process.  $\sigma_0$  is the total atomic cross section, and  $\sum_{C_S(i_1, \dots, i_l)}$  represents the sum over all possible choices of  $l$  integers (ranging from 1 to  $S$ ) out of  $S$ .

The complete cross section may be obtained, by inverting Eq. 5, from the formula

$$\begin{aligned}\sigma(A; 1, 2, \dots, S) &= \sigma_0(A) + \sum_{C_S(i_1)} \sigma_1(A; i_1) \\ &\quad + \sum_{C_S(i_1, i_2)} \sigma_1(A; i_1, i_2) + \dots \\ &\quad + \sum_{C_S(i_1, \dots, i_{S-1})} \sigma_1(A; i_1, \dots, i_{S-1}) + \sigma_1(A; 1, 2, \dots, S)\end{aligned}\quad (6)$$

The quantity of interest is the ratio

$$\chi(A; 1, 2, \dots, S) = \frac{\sigma(A; 1, 2, \dots, S) - \sigma_0(A)}{\sigma_0(A)}\quad (7)$$

Introducing the definition

$$\gamma^{(n)}(A; i_1, \dots, i_n) = \frac{\sigma_1(A; i_1, \dots, i_n)}{\sigma_0(A)}\quad (8)$$

$\chi$  is finally expressed as a sum of "normalized"  $n$ -body irreducible contributions,

$$\begin{aligned}\chi(A; 1, 2, \dots, S) &= \sum_{C_S(i_1)} \gamma^{(2)} + \sum_{C_S(i_1, i_2)} \gamma^{(3)} + \dots \\ &\quad + \sum_{C_S(i_1, \dots, i_{S-1})} \gamma^{(S-1)} + \gamma^{(S)}\end{aligned}\quad (9)$$

where, for short, the argument of the quantities  $\gamma^{(n)}$  is understood.

The approach implemented in the GNXAS package is completely self-contained and allows the computation of the theoretical model signal,  $\chi_{TH}$ , starting from a given geometrical atomic configuration around the absorber (cluster). By comparison with experimental data, the model signal is then subjected to a refinement procedure (fit), obtained by varying the structural parameters, defining the geometry of the cluster, around the starting values assumed by them in the initial configuration. In principle, changes of the geometry during the refinement procedure may affect the model potential and through it the form and the expression of the

back-scattering amplitudes and of the associated phase shifts. It will be assumed that the starting structural model is sufficiently close to the “real” situation, so that geometrical changes during the minimization will not affect back-scattering amplitudes and phase shifts, which will then be calculated once and for all at the beginning of the simulation.

Given a defined structural model around the absorber, the program starts by selecting the so-called prototypical atoms, i.e., the scatterers that within a given tolerance differ from each other in atomic number, types of neighbors, and distances from the absorber, and build, the inequivalent two-, three-, and four-body photoelectron pathways (sometimes called peaks) with which corresponding two-, three-, and four-body contributions,  $\gamma^{(2)}$ ,  $\gamma^{(3)}$ , and  $\gamma^{(4)}$ , are associated. (Higher order contributions are negligibly small in all cases we have examined.) These are listed in an output table. In general, mostly in the case of disordered systems, the number of different peaks identified with this procedure is impossibly large. To reduce their number,  $\gamma^{(n)}$ 's with similar leading frequencies are grouped together in a single term, weighted by an effective multiplicity factor.

Taking into account the geometrical relationships existing among two-, three-, and four-body configurations, one can easily count the number of independent parameters appearing in the phenomenological formula for the absorption coefficient, which will have to be varied during the minimization to fit the experimental data.

We describe below the number and type of parameters on which the various  $\gamma$ 's are actually depending. The atoms involved in a two-body configuration are the absorber, A, and a scatterer, say  $S_i$ . The corresponding peak is completely described when the distance,  $R_{AS_i}$ , between the absorber and the scatterer, the type of scatterer, and the multiplicity,  $N$ , of the configuration are given together with a specific form of the Debye-Waller (DW) factor, that takes into account all possible (static and/or dynamic) fluctuations of the scatterer position with respect to the absorber. We used a Gaussian distribution characterized by a single parameter, the width  $\sigma_{DW}$ .

One could think of improving the quality of the fit by introducing an extra parameter ( $\beta$ , in the notation of Filipponi et al., 1995a) to describe the possible asymmetry of the bond length distribution function. However, probably because of both the limited extension of the  $k$  range of our data and the strong correlation between  $R_{AS_i}$  and  $\beta$ , the  $\chi^2$  of the fit turned out to be practically insensitive to the inclusion of  $\beta$ , to the point that it was impossible to determine the skewness of the distribution, even for the first shell data.

In three-body configurations, where beside the absorber, two different scatterers,  $S_i$  and  $S_j$ , are involved, the atomic geometry can be described in terms of the lengths of the two “short” bonds,  $R_{AS_i}$  and  $R_{AS_j}$ , and the angle between them,  $\theta_{AS_iS_j}$ . The nonindependent  $R_{AS_j}$  distance (with  $R_{AS_j} > R_{AS_i}$ ) is usually referred as the “long” bond. The DW widths, associated with the “short” bonds and the angle between them, and the multiplicity of the configuration must also be given. Obviously, not all of the parameters

listed above are independent of ones entering in the two-body configurations, as  $R_{AS_i}$  and the corresponding DW width have already appeared in two-body configurations. This means that for each independent three-body contribution, only five new free parameters need to be introduced in the simulation.

The geometry of the four-body configurations is completely fixed by the parameters already considered in the two- and three-body configurations contained in it, except for its multiplicity. The latter cannot be deduced from configurations with lower number of atoms. In fact, because of the large distance from the absorber of some of the atoms involved in the signal,  $N$  cannot simply be taken as a number representing the degeneracy of the configuration (i.e., number of configurations with similar structural parameters), but rather must be taken as an effective parameter that should also account, at least partially, for the nonnegligible mobility (“disorder”) of the configuration.

Once the relevant  $n$ -body signals have been selected, the simulated signal is built by summing up, one after the other, the various contributions, starting from the largest ones. At each step of this summation, a fit is performed.

The sum will be stopped, and the remaining contributions neglected, when a sufficiently good agreement of the simulated signal with experimental data is obtained, provided also that the values of the parameters are in reasonable agreement with the assumed overall geometric arrangement.

Model clusters of astacin and thermolysin around the metal were built using the atomic coordinates extracted from crystallographic data (Matthews et al., 1972; Bode et al., 1992). (Minor but detectable differences between the structures coming from 3D diffraction measurements on crystals and that seen in experiments on samples in solution are expected. In fact, in diluted samples the long-range order constraints typical of the crystalline state are lost, and the molecular structure relaxes in a more disordered state. The tolerance interval must be sufficiently large to incorporate this effect.)

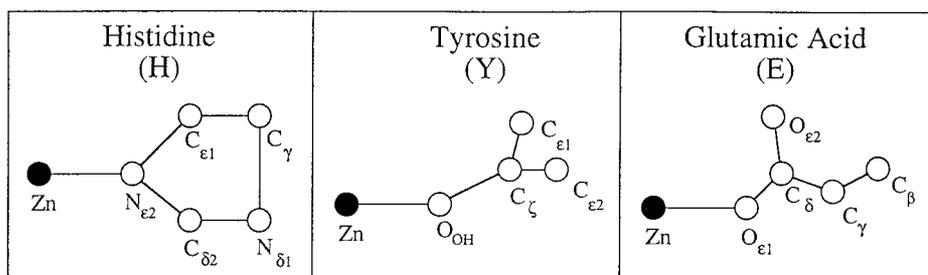
Within a cutoff distance of  $\sim 4.5$  Å, the Zn thermolysin cluster includes 15 scatterers, related to the two histidines, the glutamic acid, and the water molecule coordinated to the metal. More in detail, we have 10 atoms from the imidazole rings of the two histidines, four from the glutamic acid, and one from the water molecule. The Zn astacin cluster is formed by 20 atoms from the three histidines, the tyrosine, and the water molecule coordinated to the metal. In this case we have 15 atoms from the imidazole rings of the three histidines, four from the tyrosine, and one from the water molecule. The specific atoms belonging to the Zn-coordinated histidine, tyrosine, and glutamic acid residues that are included in the two clusters are shown in Fig. 1.

## RESULTS

### Model compounds

The spectra of the two structurally known Zn-endopeptidases, thermolysin and astacin, have been measured and

FIGURE 1 Sketch of the atomic structure of the three types of amino acidic residues (histidine, glutamic acid, and tyrosine) bound to the Zn active site. The figure shows the atoms that have been considered in the construction of the various clusters. Atoms are labeled according to the Protein Data Bank conventions.



fitted with the twofold purpose 1) of testing the ability of the present MS phenomenological analysis to recognize the nature of the amino acid residues that are bound to the metal absorber in a protein; 2) of establishing a correspondence between certain general properties of MS signals and the amino acid residues from which they originate. This specific information will be crucial to obtaining a sufficiently good and significative fit when dealing with structurally unknown compounds, as in the case of TeNT, which is of interest here.

In Fig. 2 we plot the raw spectra of thermolysin, astacin, and TeNT, where the absorbance coefficient (Eq. 1) is plotted versus the photoelectron energy expressed in eV. Fig. 3 shows the results of the fit to thermolysin and astacin data. In panels *a*, the independent  $\gamma^{(n)}$  contributions we have included in the fit are reported separately, weighted with their multiplicity factors. Six different contributions are selected by the program for thermolysin, and seven for astacin.

The independent  $\gamma^{(n)}$  are summed up, and the total simulated signal (*dotted line*), superimposed on the experimental points, is shown in panels *b*. The experimental data as well as the simulated signals have been multiplied by  $k$  to compensate for their rapid decrease with increasing  $k$ .

At the bottom of the figure the residual signal

$$k\chi_{\text{RES}}(k) = k(\chi_{\text{EXP}}(k) - \chi_{\text{TH}}(k)) \quad (10)$$

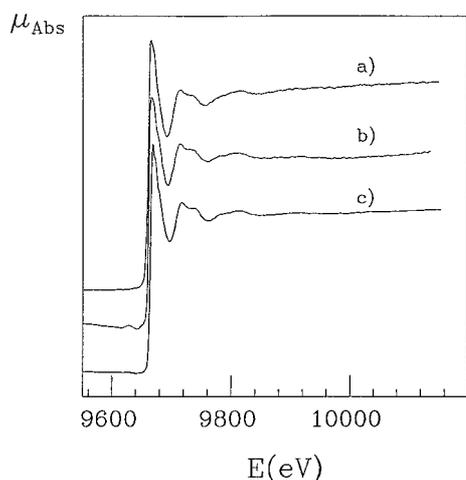


FIGURE 2 Raw XAS data for (a) thermolysin, (b) astacin, and (c) TeNT.  $\mu_{\text{ABS}}(E)$  (see Eq. 1) is plotted against the photon energy,  $E$ , expressed in electronvolts.

is plotted against  $k$ .

The values of the parameters, reported in Tables 1, 2, and 3, are obtained by minimizing the quantity

$$R = \frac{M}{M - P} \frac{\sum_k (\mu_{\text{EXP}}(k) - \mu_{\text{TH}}(k))^2}{\sum_k (\mu_{\text{EXP}}(k))^2} \quad (11)$$

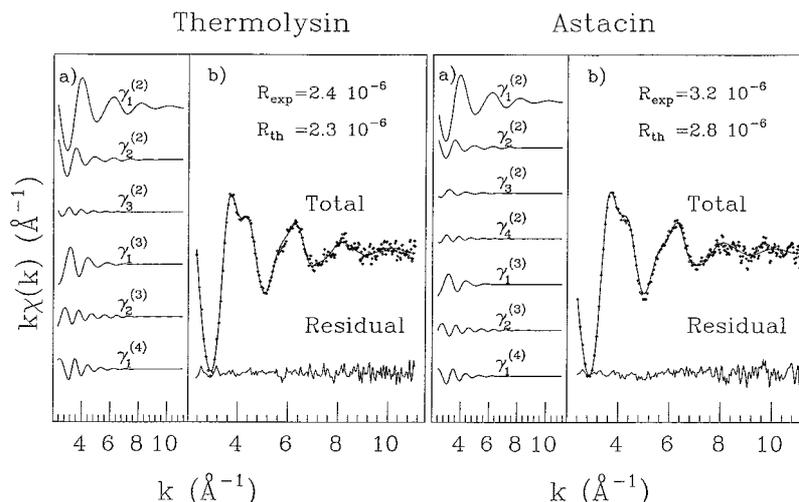
where the sum is over the  $M$  measured values of  $k$ , and  $P$  is the number of free parameters in  $\mu_{\text{TH}}$ . The normalization of  $R$  in Eq. 11 is chosen so as to allow, if necessary, the comparison of different sets of experimental data. The best fit value of  $R$ ,  $R_{\text{EXP}}$ , and the expected value,  $R_{\text{TH}}$ , defined as the value corresponding to a 95% confidence level (Filipponi et al., 1995b), assuming that  $R$  is a  $\chi^2$  distributed statistical variable, are also given in the figure. Comparable values of  $R_{\text{EXP}}$  and  $R_{\text{TH}}$  should be found for acceptably good fits. In Table 1 we report the best fit values of the parameters of the two-body contributions,  $\gamma^{(2)}$ . In the second column we give the atoms identifying the photoelectron pathways of the various contributions. Next to each atom we indicate, in parentheses, the amino acid residue to which they belong. No special label has been given to the coordinated water oxygen. In the third, fourth, and fifth columns we report the distance between the absorber and the scatterer,  $R_{\text{ASi}}$ , the corresponding DW width,  $\sigma_{\text{DW}}$ , and the multiplicity of the configuration,  $N$ . The errors on all parameters are on the last digit and are given in parentheses.

In the last three columns, numbers extracted from crystallographic data are listed for comparison. The values reported in the sixth column are obtained by averaging the crystallographic distances of the  $N_X$  pairs of atoms listed in the second column. The quantity we suggest to compare with  $\sigma_{\text{DW}}$  is the standard deviation of the averaged atomic distances. Standard deviations are reported in the seventh column.

We see that XAS and crystallographic results show a good overall degree of consistency. Minor discrepancies should be attributed to the structural differences that certainly exist between the crystalline and the liquid phase of the sample.

It should be noted that the DW widths attributed to the XAS parameters on the basis of the theoretical treatment we are using here account for both static and dynamic disorder. On the other hand, the standard deviations computed from crystallographic data are only sensitive to static disorder. As a consequence, when the scatterers are firmly bound to the absorber (as in the case of the nearest covalently bonded

FIGURE 3 Results of the best fits on thermolysin (left) and astacin (right) data. (a)  $n$ -body independent contributions considered in the fit. (b) The total simulated signals (dotted line) are superimposed on the experimental points. At the bottom of panels b, we plot the residual functions (see Eq. 10). The values of  $R_{\text{EXP}}$  and  $R_{\text{TH}}$  are reported as a measure of the goodness of the fit. All curves and data points are multiplied by corresponding values of the photon momentum  $k$  (see text).



atoms), the static disorder is dominant and the two parameters are almost identical. For more distant atoms, which can move more freely with respect to the absorber, static and dynamic contributions may lead to DW widths very different from the corresponding crystallographic standard deviations.

Table 2 shows the best fit values of the parameters of the three-body contributions,  $\gamma^{(3)}$ . The atoms involved in the three-body pathways are listed in the second column, and in the following four columns we report the lengths of the short bond,  $R_{\text{SiSj}}$  (the  $R_{\text{ASi}}$ 's are the same as for the  $\gamma^{(2)}$  contributions); the angle,  $\theta_{\text{ASiSj}}$ , between  $R_{\text{ASi}}$  and  $R_{\text{SiSj}}$ ; the length of the so-called long bond,  $R_{\text{long}}$ ; and the multiplicity factors,  $N$ . The DW widths are reported below the value of the physical quantity they refer to. It should be recalled that the length,  $R_{\text{long}}$ , and the associated DW width, given in the seventh column, are not free parameters, but they are computed by the program in terms of the distances, angles, and DW widths on which they depend.

In the last three columns the mean values of  $R_{\text{long}}$ ,  $\theta_{\text{ASiSj}}$  and the corresponding standard deviations, as obtained from crystallographic data in the way explained before, are given for comparison. As before,  $N_{\text{X}}$  is the number of pathways listed on the second column.

Because of the rapid convergence of the  $n$ -body expansion, four-body contributions are usually not included in the theoretical formulae, except when four-body quasicolinear configurations are present, because in this case they are known to give rise to quite large contributions, comparable with the three-body terms of the same path length (Blackburn et al., 1983). In thermolysin and astacin the Zn absorber is known to be coordinated to two or three histidine residues, respectively, by a nitrogen atom of the imidazole ring. Given the rigid geometry of the imidazole ring, two almost colinear pathways for each bound histidine are clearly identified. In fact, as can be seen from the results reported in Fig. 3, four-body contributions turn out not to be small and cannot be neglected, once three-body signals

TABLE 1 Values of the parameters entering in the two-body signals,  $\gamma^{(2)}$ , plotted in Fig. 3

Atomic pathway	EXAFS			X-ray diffraction			
	$R_{\text{ASi}}$ (Å)	$\sigma_{\text{DW}}$ (Å)	$N$	$\langle R \rangle$ (Å)	$\sigma$ (Å)	$N_{\text{X}}$	
Thermolysin							
$\gamma_1^{(2)}$	Zn-N <sub>e2</sub> (H1, H2), Zn-O <sub>e1</sub> (E), Zn-O	1.98 (1)	0.084 (3)	3.6 (2)	2.04	0.09	4
$\gamma_2^{(2)}$	Zn-C <sub>e1</sub> (H1, H2), Zn-C <sub>82</sub> (H1, H2), Zn-C <sub>8</sub> (E), Zn-O <sub>e2</sub> (E)	3.05 (3)	0.14 (1)	6.0 (5)	2.9	0.2	6
$\gamma_3^{(2)}$	Zn-C <sub>γ</sub> (H1, H2), Zn-N <sub>81</sub> (H1, H2), Zn-C <sub>γ</sub> (E)	4.4 (1)	0.15 (2)	5.3 (5)	4.2	0.1	5
Astacin							
$\gamma_1^{(2)}$	Zn-N <sub>e2</sub> (H1, H2, H3), Zn-O	1.98 (1)	0.087 (3)	4.0 (2)	2.07	0.07	4
$\gamma_2^{(2)}$	Zn-C <sub>e1</sub> (H1, H2), Zn-C <sub>82</sub> (H1, H2), Zn-O <sub>OH</sub> (Y)	3.02 (3)	0.13 (1)	4.0 (5)	2.9	0.2	5
$\gamma_3^{(2)}$	Zn-C <sub>e1</sub> (H3), Zn-C <sub>82</sub> (H3), Zn-C <sub>ε</sub> (Y)	3.32 (5)	0.14 (2)	2.2 (5)	3.3	0.1	3
$\gamma_4^{(2)}$	Zn-C <sub>γ</sub> (H1, H2, H3), Zn-N <sub>81</sub> (H1, H2, H3), Zn-C <sub>e1</sub> (Y)	4.4 (1)	0.15 (2)	6.1 (5)	4.2	0.1	7

Hi stands for histidine (1, 2, or 3), E for glutamic acid, and Y for tyrosine, and the oxygen belonging to the coordinated water molecule is left unlabeled. The atoms are named after the Protein Data Bank conventions.

**TABLE 2** Three-body signals,  $\gamma^{(3)}$ 

Atomic pathway	EXAFS				X-ray diffraction			
	$R_{S_iS_j}$ (Å) $\sigma_{DW}$ (Å)	$\theta_{AS_iS_j}$ (deg) $\sigma_{DW}$ (deg)	$R_{long}$ (Å) $\sigma_{DW}$ (Å)	$N$	$\langle R_{long} \rangle$ (Å) $\sigma$ (Å)	$\langle \theta_{AS_iS_j} \rangle$ (deg) $\sigma$ (deg)	$N_X$	
Thermolysin								
$\gamma_1^{(3)}$	Zn-N $_{e2}$ -C $_{\delta 2}$ (H1, H2),	1.30 (3)	129 (10)	2.97	6.0 (5)	2.9	123	6
	Zn-N $_{e2}$ -C $_{e1}$ (H1, H2)	0.11 (1)	3 (1)	0.13		0.2	9	
	Zn-O $_{e1}$ -C $_{\delta}$ (E)							
	Zn-O $_{e1}$ -O $_{e2}$ (E)							
$\gamma_2^{(3)}$	Zn-N $_{e2}$ -C $_{\gamma}$ (H1, H2),	2.25 (6)	165 (5)	4.2	5.0 (5)	4.1	162	5
	Zn-N $_{e2}$ -N $_{\delta 1}$ (H1, H2),	0.13 (1)	3 (1)	0.15		0.1	8	
	Zn-O $_{e1}$ -C $_{\gamma}$ (E)							
Astacin								
$\gamma_1^{(3)}$	Zn-N $_{e2}$ -C $_{e1}$ (H1, H2, H3)	1.30 (5)	128 (10)	2.96	5.4 (5)	2.9	126	6
	Zn-N $_{e2}$ -C $_{\delta 2}$ (H1, H2, H3)	0.14 (1)	5 (1)	0.15		0.2	5	
$\gamma_2^{(3)}$	Zn-N $_{e2}$ -C $_{\gamma}$ (H1, H2, H3)	2.30 (6)	162 (5)	4.2	5.2 (5)	4.2	160	6
	Zn-N $_{e2}$ -N $_{\delta 1}$ (H1, H2, H3)	0.12 (1)	6 (1)	0.15		0.1	5	

Same as Table 1.

involving the atoms of the imidazole ring have been included in the fitting formula.

In Table 3 we list next to the name of the atoms involved in the four-body contribution the length of the “long” bond,  $R_{long}$ , with its DW width and multiplicity factor,  $N$ . The length of the bonds and the magnitude of the angles that define the geometry of the four-body pathways have been taken either as being the same as those of lowest order contributions ( $\gamma^{(2)}$  and/or  $\gamma^{(3)}$ ) or have held fixed to their crystallographic values. As a consequence, the only new parameter of the four-body configurations is their multiplicity,  $N$ . In the last three columns we report the crystallographic mean values of  $R_{long}$  with its standard deviation and the number of atoms over which the average has been made.

We now wish to briefly comment on the quality of the fits and on the physical interpretation of the results we have found.

Looking at Tables 1, 2, and 3, we conclude that in the case of thermolysin there is a very good agreement between the crystallographic parameters and the values we get from

the fit to XAS data. It should be stressed that our analysis has allowed a separate identification of the contributions specifically coming from the atoms belonging to the histidines and the glutamic acid and of those coming from the oxygen of the water molecule. This observation will be important in the discussion of our fitting strategy in the case of TeNT.

As for the fit to astacin data, the first thing that may be noted is that multiplicities are systematically lower than expected from crystallography, even in the two-body contributions in which multiplicities should coincide with coordination numbers (i.e., with the number of atoms at binding distances from the absorber), because in these signals single scattering events are dominant. This trend can be explained by recalling that the fifth ligand of Zn in astacin, the tyrosine residue, is hindered by steric constraints. In fact, the tyrosine oxygen, O $_{OH}$ , which is assumed to be coordinated to the metal site, is found, by crystallographic data, at a distance of 2.52 Å, well beyond a standard Zn-O coordination distance. Furthermore, as the distances of the

**TABLE 3** Four-body signals,  $\gamma^{(4)}$ 

Atomic pathway	EXAFS			X-Ray Diffraction			
	$R_{long}$ (Å)	$\sigma_{DW}$ (Å)	$N$	$\langle R_{long} \rangle$ (Å)	$\sigma$ (Å)	$N_X$	
Thermolysin							
$\gamma_1^{(4)}$	Zn-N $_{e2}$ -C $_{\gamma}$ -C $_{e1}$ (H1, H2)	4.1	0.15	3.7 (5)	4.2	0.1	4
	Zn-N $_{e2}$ -N $_{\delta 1}$ -C $_{\delta 2}$ (H1, H2)						
Astacin							
$\gamma_1^{(4)}$	Zn-N $_{e2}$ -C $_{\gamma}$ -C $_{e1}$ (H1, H2)	4.1	0.09	3.9 (5)	4.2	0.1	4
	Zn-N $_{e2}$ -N $_{\delta 1}$ -C $_{\delta 2}$ (H1, H2)						

Same as Table 1.

three histidines are smaller in average in a liquid than in a crystal (see the data of the  $\gamma_1^{(2)}$  contributions in Table 1), the steric hindrance problem of the tyrosine is stronger in our case, as we are dealing with a liquid sample and not with a crystal, as in x-ray diffraction experiments. Consequently, the tyrosine residue, being forced to stay somewhat further away from the metallic site, is less strongly bound to the Zn and can move more freely, thus increasing the “disorder” of the configurations. Increasing the disorder gives rise to a systematic lowering of the resulting values of coordination numbers (Lee et al., 1981), as observed in the parameters of the  $\gamma^{(2)}$  contributions.

Another general remark about the astacin results is that four types of two-body signals were required in the fit, instead of the three necessary in the thermolysin case. This is again due to the “crowding” of amino acids around Zn. This circumstance, besides having the effect of pushing away the tyrosine, also gives rise to a distortion of the geometry of one of the three histidines, so that the different pathways initially generated by the program cannot be grouped into only three contributions. This follows from the fact that some atoms of the tyrosine and of the histidine are pushed at intermediate distances between the second shell (3 Å) and the third one (4 Å). This structural pattern is clearly visible also in the crystallographic data.

Concerning three-body terms, it appears from Table 2 that in all of the  $\gamma^{(3)}$  signals of the astacin, only the atoms of the histidine residues are involved, whereas in thermolysin atoms belonging to the glutamic acid also had to be considered. The coordination number of the three-body signal is lower than the expected value (which is 6, as there are two contributing atoms from each histidine), thus supporting the previous picture of one of the histidines being somewhat distorted.

We already remarked that the  $\gamma^{(4)}$  contributions have been built using the values of the geometrical parameters coming from the lowest order contributions, the only new parameter being the multiplicity. As expected (see the second column of Table 3), only the atoms of the histidine residues are involved in the atomic pathways of the quasi-collinear four-body configurations contributing to  $\gamma^{(4)}$ . A final observation is that in the astacin case, no contribution is seen from the third coordinated histidine. This is confirmed by the consistency of the crystallographic data on  $R_{\text{long}}$  obtained by averaging only over the atoms of the two undistorted histidines.

In conclusion, the quality of the fit we have obtained in the case of both thermolysin and astacin, and the overall consistency we find between the XAS geometrical parameters and the available crystallographic data, are extremely encouraging and lead us to conclude that our refined MS analysis has the potential of allowing the complete identification of the amino acid residues bound to an active metallic site, even in the case of structurally unknown metalloproteins.

## Tetanus neurotoxin

We start by giving a brief description of the strategy we followed to fit the TeNT experimental data in light of the experience we gained from fitting thermolysin and astacin EXAFS spectra.

Biochemical (Schiavo et al., 1992a) and mutagenesis (Yamasaki et al., 1994) experiments clearly indicate that, besides water, two and only two histidines are coordinated to Zn in TeNT. Furthermore, based on the single scattering analysis of the EXAFS region, it was argued by Morante et al. (1996) that the structure of the active site in TeNT was intermediate between that of thermolysin and that of astacin.

Then the questions that remain to be assessed are 1) the number (one or two) of further possible coordinated amino acids and 2) the nature (tyrosine and/or glutamic acid) of these residues.

The results obtained by fitting thermolysin and astacin data have allowed a precise identification of the atomic pathways that give rise to the various  $\gamma^{(n)}$  signals. This means, in practice, that we know for each amino acid residue bound to the absorber which  $\gamma^{(n)}$  signal contributes to the EXAFS signal.

Guided by the experimental indication that TeNT is structurally not too different from thermolysin and astacin, we tried a fit to the TeNT data by using the set of  $\gamma$ 's previously identified in fitting the spectra of the two enzymes. After a certain number of trials, we ended up with the best fit parameters shown in Table 4, which give rise to the curves shown in Fig. 4. The first thing to notice is the absence of a fourth  $\gamma_4^{(2)}$  signal, which was instead necessary to fit astacin data, as explained before. This immediately signals that no particularly strong steric problems are experienced

**TABLE 4** Values of the parameters entering in the two-, three-, and four-body signals,  $\gamma^{(2)}$ ,  $\gamma^{(3)}$ , and  $\gamma^{(4)}$ , plotted in Fig. 4

Two-body					
	$R_{\text{As}_i}$ (Å)	$\sigma_{\text{DW}}$ (Å)	$N$		
$\gamma_1^{(2)}$	1.98 (1)	0.087 (3)	4.1 (2)		
$\gamma_2^{(2)}$	3.04 (5)	0.14 (1)	5.0 (5)		
$\gamma_3^{(2)}$	4.4 (1)	0.15 (1)	6.0 (5)		
Three-body					
	$R_{\text{S}_i\text{S}_j}$ (Å)	$\theta_{\text{As}_i\text{S}_j}$ (deg)	$R_{\text{long}}$ (Å)	$\sigma_{\text{DW}}$ (Å)	$N$
	$\sigma_{\text{DW}}$ (Å)	$\sigma_{\text{DW}}$ (deg)			
$\gamma_1^{(3)}$	1.30 (5)	129 (8)	2.96	0.11	5.0 (5)
	0.09 (1)	3 (1)			
$\gamma_2^{(3)}$	2.26 (5)	166 (8)	4.2	0.13	5.0 (5)
	0.10 (1)	5 (1)			
Four-body					
	$R_{\text{long}}$ (Å)	$\sigma_{\text{DW}}$ (Å)	$N$		
$\gamma_1^{(4)}$	4.2	0.15	3.9 (5)		

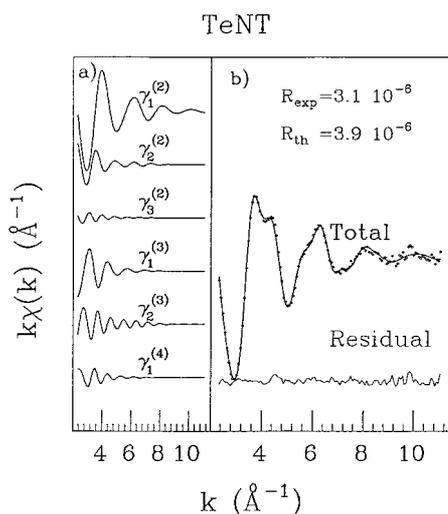


FIGURE 4 Results of the best fit to the TeNT data (see caption of Fig. 3 for notation).

by any of the coordinated residues, thus hinting toward having only one extra coordinated amino acid besides the basic two histidines—one water molecule component.

To physically interpret the results we have obtained, we compare the values of the geometrical parameters of Table 4 with those of the two model compounds. For reasons that will be immediately clear, let us analyze separately the results on bond lengths and angles on one side, and those on the multiplicities on the other.

We first note that the best fit values of the  $\gamma^{(2)}$  parameters coincide, within errors, with those of thermolysin (see Table 2 for comparison), whereas they differ significantly from those of astacin.

In the case of  $\gamma^{(3)}$  and  $\gamma^{(4)}$ , the parameters of TeNT fit do not differ appreciably from the very similar values they take in the two other enzymes.

The situation is much more interesting if one looks at the values of the multiplicity factors, because they are remarkably different from those of both thermolysin and astacin, and allow us to discriminate among different possible coordination patterns.

To analyze these differences, in Table 5 we report the numbers of possible pathways with which each amino acidic residue should contribute to the multiplicity of each signal. In the first row of the upper panel we list the contributions to the multiplicity coming from the basic configuration of two histidines plus a water molecule. In the following four rows the contributions of glutamic acid and tyrosine residues are given. Glutamic acid and tyrosine have been considered in two alternative positions with respect to the absorber: the so-called far and near positions, depending on whether Zn is supposed to be penta- or tetraordinated, respectively.

In the lower panel we report for each  $\gamma$  the total multiplicity that characterizes the various possible alternative configurations. These may be separated into two tetraoor-

TABLE 5 Multiplicity factors

	$\gamma_1^{(2)}$	$\gamma_2^{(2)}$	$\gamma_3^{(2)}$	$\gamma_1^{(3)}$	$\gamma_2^{(3)}$	$\gamma_1^{(4)}$
2H + O	3	4	4	4	4	4
E <sub>near</sub>	1	2	1	1	1	0
E <sub>far</sub>	0	1	2	0	1	0
Y <sub>near</sub>	1	1	2	1	1	0
Y <sub>far</sub>	0	1	1	0	1	0
2H + O + E <sub>near</sub>	4	6	5	5	5	4
2H + O + Y <sub>near</sub>	4	5	6	5	5	4
2H + O + E <sub>near</sub> + Y <sub>far</sub>	4	7	6	5	6	4
2H + O + E <sub>far</sub> + Y <sub>near</sub>	4	6	8	5	6	4
2H + O + E <sub>near</sub> + Y <sub>near</sub>	5	7	7	6	6	4

Upper panel: Contribution to the multiplicity of the basic configuration of two histidines plus a water molecule (second row) and, in the two alternative “near” and “far” positions, of glutamic acid (third and fourth rows) and of tyrosine (fifth and sixth rows). Lower panel: Overall multiplicity of the five alternative bonding configurations around the Zn in TeNT.

ordinated and three pentacoordinated configurations (as we said, two histidines and a water molecule are known to be bound to the Zn). The tetraordinated configuration may have an extra glutamic acid (first row) or an extra tyrosine (second row) residue. The pentacoordinated Zn may be obtained by having either a “near” tyrosine plus a “far” glutamic acid (third row) or a “far” tyrosine plus a “near” glutamic acid (fourth row). In the last row we also consider a pentacoordinated Zn with both residues, tyrosine and glutamic acid, “near” the absorber. In fact, the absence of the third histidine, with its “big” imidazole ring, may actually allow the five ligands to be not too distant from Zn.

Comparing these multiplicity numbers with those of Table 4, we clearly see that the only set of multiplicities that is compatible with the best fit values of Table 4 is the one that corresponds to the Zn active site being bound to a tyrosine as a fourth ligand besides two histidines and a water molecule.

## CONCLUSIONS AND OUTLOOKS

In this paper we have shown that x-ray absorption spectroscopy can be profitably used to study the environment of the active site of metalloproteins.

An accurate theoretical analysis of the near edge and EXAFS regions of the spectrum in terms of single and multiple scattering contributions allows a clear-cut identification of the amino acid residues primarily bound to the metal.

Besides reproducing the known atomic structure around Zn in thermolysin and astacin, we have been able to completely determine the coordination mode of Zn in TeNT.

The results reached in the present investigation are extremely encouraging and lead us to believe that this spectroscopic technique, associated with the refined theoretical analysis developed in the papers of Benfatto et al. (1986) and Filipponi et al. (1995a), are of invaluable help in answering questions where the knowledge of the atomic structure around a protein active site is a prerequisite for the

understanding of the biological mechanisms underlying protein enzymatic activity.

For the future we envisage moving in two directions. The first line of research has to do with the recent idea (Cavatorta et al., 1994) that the formation of Zn-MBP (myelin basic protein) complexes in the presence of phosphate ions might be at the origin of the reported substantial reduction of the demyelination process rate in *in vitro* experiments. In view of the possible therapeutic relevance of this observation, it is of the utmost importance to arrive at a clear determination of the atomic environment around Zn, when these aggregates are formed, to understand the nature of the biochemical mechanisms responsible for the possible blockage of demyelination processes.

The second project consists of performing measurements of the calcium (Ca) EXAFS spectrum in calciocalsestrin, a natural Ca reservoir (Franzini-Armstrong et al., 1987) capable of binding up to 50 Ca ions, which is also known to play a catalytic role in the activity of Ca release channels. The experiment should be able to clarify the peculiar Ca binding mode and may shed light on the catalytic properties of calciocalsestrin, by determining the geometric atomic arrangement around the metallic binding site.

We thank C. R. Natoli and G. C. Rossi for discussions and for a careful reading of the manuscript. We also thank F. Campolungo, V. Sciarra, and V. Tullio (Laboratori Nazionali di Frascati, Italy) for technical support.

Partial financial support from INFM and CNR, Italy, is gratefully acknowledged.

## REFERENCES

- Ashley, C. A., and S. Doniach. 1975. Theory of the extended X-ray absorption fine structure (EXAFS) in crystalline solids. *Phys. Rev. B.* 11:1279–1288.
- Baumann, U., S. Wu, K. M. Flaherty, and D. B. McKay. 1993. Three-dimensional structure of the alkaline protease of *Pseudomonas aeruginosa*: a two-domain protein with calcium binding parallel beta roll motif. *EMBO J.* 12:3357–3364.
- Benfatto, M., C. R. Natoli, A. Bianconi, J. Garcia, A. Marcelli, M. Fanfoni, and I. Davoli. 1986. Multiple scattering regime and higher-order correlations in x-ray absorption spectra of liquid solutions. *Phys. Rev. B.* 34:5774–5781.
- Bianconi, A., A. Di Cicco, N. V. Pavel, M. Benfatto, A. Marcelli, C. R. Natoli, P. Pianetta, and J. Woicik. 1987. Multiple-scattering effects in the K-edge x-ray absorption near-edge structure of crystalline and amorphous silicon. *Phys. Rev. B.* 36:6426–6433.
- Blackburn, N. J., S. S. Hasnain, G. P. Diakun, P. F. Knowles, N. Binsted, and C. D. Garner. 1983. An extended x-ray absorption fine structure study of the copper and zinc sites of freeze-dried bovine superoxide dismutase. *Biochem. J.* 213:765–768.
- Bode, W., F. X. Gomis-Ruth, R. Huber, R. Zwillig, and W. Stocker. 1992. Structure of astacin and implications for activation of astacins and zinc-ligation of collagenases. *Nature.* 358:164–167.
- Bunker, G., E. A. Stern, R. E. Blankenship, and W. W. Parson. 1982. An x-ray absorption study of the iron site in bacterial photosynthetic reaction center. *Biophys. J.* 37:539–551.
- Cavatorta, P., S. Giovannelli, A. Bobba, P. Riccio, and E. Quagliarello. 1994. Myelin basic protein interaction with Zn and phosphate: fluorescence studies on the water-soluble form of the protein. *Biophys. J.* 66:1174–1179.
- Cramer, S. P. 1988. X-Ray Absorption: Principles, Applications, Techniques of EXAFS and XANES. John Wiley and Sons, New York. 573–662.
- Filippini, A., A. Di Cicco, and C. R. Natoli. 1995a. X-ray absorption spectroscopy and *n*-body distribution functions in condensed matter. I. Theory. *Phys. Rev. B.* 52:15122–15134.
- Filippini, A., A. Di Cicco, and C. R. Natoli. 1995b. X-ray absorption spectroscopy and *n*-body distribution functions in condensed matter. II. Data analysis and applications. *Phys. Rev. B.* 52:15135–15149.
- Filippini, A., F. Evangelisti, M. Benfatto, S. Mobilio, and C. R. Natoli. 1989. Structural investigation of a-Si and a-Si:H using x-ray absorption spectroscopy at the Si K-edge. *Phys. Rev. B.* 40:9636–9643.
- Fonda, L. 1992. Multiple-scattering theory of x-ray absorption: a review. *J. Phys. Condens. Matter.* 4:8269–832.
- Franzini-Armstrong, C., L. J. Kenney, and E. Varriano-Marston. 1987. The structure of calciocalsestrin in triads of vertebrates skeletal muscle: a deep-etch study. *J. Cell Biol.* 105:49–56.
- Gurman, S. J., N. Binsted, and I. Ross. 1986. A rapid, exact, curved-wave theory for EXAFS calculations. II. The multiple-scattering contributions. *J. Phys. C.* 19:1845–1861.
- Koningsberger, D. C., and R. Prins. 1988. X-Ray Absorption. John Wiley and Sons, New York.
- Lebeda, J. J., and M. A. Olson. 1994. Secondary structural predictions for the clostridial neurotoxins. *Proteins Struct. Funct. Genet.* 20:293–300.
- Lee, P. A., P. Citrin, P. Eisenberger, and B. Kincaid. 1981. Extended x-ray absorption fine structure—its strengths and limitations as a structural tool. *Rev. Mod. Phys.* 53:769–806.
- Lee, P. A., and J. B. Pendry. 1975. Theory of the extended x-ray absorption fine structure. *Phys. Rev. B.* 11:2795–2811.
- Matthews, B. W., J. N. Jansonius, P. M. Colman, K. Titani, K. A. Walsh, and H. Neurath. 1972. Structure of thermolysin. *Nature New Biol.* 238:37–41.
- Matsubara, H. 1970. Purification and assay of thermolysin. *Methods Enzymol.* 19:642–650.
- Minton, N. 1995. Molecular genetics of clostridial neurotoxins. In *Clostridial Neurotoxins. Curr. Top. Microbiol. Immunol.* 195:161–194.
- Montecucco, C., and G. Schiavo. 1993. Tetanus and botulinum neurotoxins: a new group of zinc proteases. *Trends Biochem. Sci.* 18:324–327.
- Montecucco, C., and G. Schiavo. 1994. Mechanism of action of tetanus and botulinum neurotoxins. *Mol. Microbiol.* 13:1–8.
- Morante, S., L. Furenlid, G. Schiavo, F. Tonello, R. Zwillig, and C. Montecucco. 1996. X-ray absorption spectroscopy study of zinc coordination in tetanus neurotoxin, astacin, alkaline protease and thermolysin. *Eur. J. Biochem.* 235:606–612.
- Pascarelli, S., F. Boscherini, F. D'Acapito, J. Hardy, C. Meneghini, and S. Mobilio. 1996. X-ray optics of a dynamical sagittal-focusing monochromator on the GILDA beam-line at the ESRF. *J. Synchrotron Rad.* 3:147–155.
- Rossetto, O., G. Schiavo, C. Montecucco, B. Poulain, F. Deloye, L. Lozzi, and C. C. Shone. 1994. SNARE motif and neurotoxin recognition. *Nature.* 372:415–416.
- Sayers, D. E., E. A. Stern, and F. W. Lytle. 1971. New technique for investigating non-crystalline structures: Fourier analysis of the extended x-ray absorption fine structure. *Phys. Rev. Lett.* 27:1204–1207.
- Schiavo, G., F. Benfenati, B. Poulain, O. Rossetto, P. Polverino de Lauroto, B. R. DasGupta, and C. Montecucco. 1992a. Tetanus and botulinum-B neurotoxins block neurotransmitter release by proteolytic cleavage of synaptobrevin. *Nature.* 359:832–835.
- Schiavo, G., O. Rossetto, A. Santucci, B. R. DasGupta, and C. Montecucco. 1992b. Botulinum neurotoxins are zinc proteins. *J. Biol. Chem.* 267:23479–23483.
- Shulman, R. G., P. Eisenberger, and B. M. Kincaid. 1978. X-ray absorption spectroscopy of biological molecules. *Annu. Rev. Biophys. Bioeng.* 7:559–578.
- Simpson, L. L. 1989. Botulinum Neurotoxin and Tetanus Toxin. Academic Press, San Diego.
- Stern, E. A. 1974. Theory of the extended x-ray absorption fine structure. *Phys. Rev. B.* 10:3027–3037.

- Strange, R. W., N. J. Blackburn, P. F. Knowles, and S. S. Hasnain. 1987. X-ray absorption spectroscopy of metal-histidine coordination in metalloproteins. Exact simulation of the EXAFS of tetrakis(imidazole)copper(II) nitrate and other copper-imidazole complexes by the use of a multiple-scattering treatment. *J. Am. Chem. Soc.* 109:7157–7162.
- Teo, B. K., and D. C. Joy. 1981. EXAFS Spectroscopy, Techniques and Applications. Plenum Press, New York.
- Zhang, H. H., A. Filipponi, A. Di Cicco, M. J. Scott, R. H. Holm, B. Hedman, and K. O. Hodgson. 1997. Multiple-edge XAS studies of cyanide-bridged iron-copper molecular assemblies relevant to cyanide-inhibited heme-copper oxidases using four-body multiple-scattering analysis. *J. Am. Chem. Soc.* 119:2470–2478.
- Zwilling, R., and H. Neurath. 1981. Invertebrate proteases. *Methods Enzymol.* 80:633–664.